Available online at www.sciencedirect.com
ScienceDirect
Journal of Sound and Vibration 317 (2008) 473–489
JOURNAL OF SOUND AND VIBRATION
www.elsevier.com/locate/jsvi

Rapid Communication

Study of a flexible disk rotating close to a rigid rotating wall considering fluid inertia effects

Abdelrasoul M.M. Gad*, Yoon Chul Rhim[1]

Center for Information Storage Device, Yonsei University, Seoul 120-749, Republic of Korea

Received 31 December 2007; received in revised form 26 May 2008; accepted 29 May 2008
Handling Editor: L.G. Tham
Available online 3 July 2008

Abstract

The present study is a numerical simulation about the dynamics of a flexible disk coupled to thin air film and rotating close to a rigid rotating wall. The idea of a flexible disk rotating in a close proximity of a rigid rotating wall is introduced and studied with two new types of flat stabilizers, co-rotating and counter-rotating flat stabilizers, besides the well-known fixed-stabilizer type which has been studied extensively in earlier works. In the present study, the flexible disk is modeled using linear plate theory and the air flow between the flexible disk and the rigid wall is modeled using Navier–Stokes and continuity equations. The flow equations are discretized using cell centered finite volume method (FVM) and solved numerically with the SIMPLE algorithm, while the spatial terms in the disk model are discretized using finite difference method (FDM) and time integration is performed using fourth-order Runge–Kutta method. The effect of inertia and coriollis forces on the disk displacement and air-film pressure is studied, also the dependence of these forces on the rotation speed, initial gap size and inlet-hole radius is investigated. A transient numerical code is developed to compare the stability boundaries for the different types of flat stabilizer at a wide range of circumferential mode numbers. The numerical results showed an improved stability of the flexible disk when rotating close to a counter-rotating flat stabilizer compared with co-rotating and fixed flat stabilizers.

1. Introduction

Flexible disks are widely used as low-cost recording medium for computer memories. The recent drastic increase in the quantity of computer data has led to a strong demand for high-speed, high-reliability devices based on flexible disks. The strong demands for high data access rates and high reliability require small transverse vibrations of the disk at high rotation speeds. So, it is important to investigate the optimal design for the flexible disk system since it is a good candidate for compact as well as high-capacity data storage means. Several studies have been carried out for the investigation of the dynamic characteristics of a flexible disk rotating close to a rigid wall both analytically and experimentally.

*Corresponding author. Tel.: +82 2 2123 2820; fax: +82 2 312 2159.
E-mail addresses: a_mahmoud1976@yahoo.com, gad76@yonsei.ac.kr (A.M.M. Gad), rhimyc@yonsei.ac.kr (Y.C. Rhim).
[1]Tel.: +82 2 2123 2820; fax: +82 2 312 2159.

0022-460X/$ - see front matter
doi:10.1016/j.jsv.2008.05.035

Nomenclature

D	bending stiffness of the disk material
E	Young's modulus of the disk material
h	disk thickness
h_o	initial gap height
J	Jacobian of transformation
m	circumferential mode number
p	fluid pressure
p_o	steady-state air-film pressure
p_a	ambient pressure
r, θ, z	cylindrical coordinates
r	radial distance
r_o	flexible disk outside radius
r_c	flexible disk clamping radius
r_h	inlet-hole radius
Re_r, Re_θ, Re_z	modified Reynolds numbers in radial, azimuthal and axial directions, respectively
t	time
v	flexible disk axial velocity
v_r, v_θ, v_z	flow velocities along the coordinates directions
v_r^o, v_θ^o, v_z^o	reference velocities (v_r^o, v_θ^o, $v_z^o = \omega r_o$)
w	flexible disk displacement
w_o	steady-state disk displacement
z	axial distance

Greek letters

ε	perturbation parameter
η, ζ, ξ	computational coordinates
μ	fluid viscosity
μ_{air}	air viscosity
ρ	fluid density
ρ_{air}	air density
ρ_d	material density of the disk
σ_r, σ_θ	steady-state stresses in the disk material in radial and circumferential directions
υ	Poisson's ratio
ω	angular velocity of the disk
∇^4	biharmonic operator

Pelech and Shapiro [1] analyzed the flow generated by the rotation of a flexible disk close to a rigid wall at low Reynolds numbers, so they neglected all convective inertia terms because of their comparatively small values. Bogy and Talke [2] obtained steady solutions for pressurized flexible disk packs using the same analytical model proposed by Pelech and Shapiro [1].

Hosaka and Crandall [3] were the first to estimate the maximum stable operating speed of a flexible disk coupled to thin air film, theoretically. In their study, they performed a single-mode analysis in order to obtain a rough estimate for the critical speed analytically. The single-mode analysis reduced the disk-film system to one homogenous linear algebraic equation which has a form identical to the characteristic equation that governs wave propagation of axially moving beam subjected to axially moving damping. The onset speed of instability predicted by the single-mode analysis was close to the speed obtained from more accurate numerical method. They found that the instability appears when the relative velocity between the disk and the average air flow in the fluid film is larger than the traveling wave velocity of the disk vibration.

D'Angelo and Mote [4] showed that the disk spinning at high supercritical rotation speed in a fluid becomes unstable by traveling wave aeroelastic flutter. At speeds below the flutter speed, the disk vibrates under unsteady pressure from the flow around the disk while at flutter and at higher speeds, the fluid and disk motions become coupled. Also, they showed that a wall positioned parallel to the disk and separated from the disk by 0.5 cm does not change the flutter speed, frequency or mode, but it increases the post-flutter frequency.

Yasuda et al. [5] performed a theoretical as well as an experimental study for the self-excited vibrations of a flexible disk rotating in air. First, they analyzed the free vibrations of the disk without the effect of air and then the vibrations of the disk in air were analyzed. The forces produced by air were considered to consist of two terms; one being an ordinary viscous damping and the other is lifting force. Their results showed that the vibrations of the disk in air propagate as forward and backward traveling waves. While, the forward traveling wave always decays, they showed that the backward traveling wave can become of a self-excited nature at rotational speeds higher than certain value.

Huang and Mote [6] presented an analytical investigation of instability mechanisms in the coupled fluid–disk system. The fluid film response was modeled using a modified Reynolds equation that includes contribution of the fluid centrifugal inertia while the disk transverse vibration was modeled as a classical

rotating plate under distributed film pressure. They concluded that the instabilities in the disk-film system are of two types; a rotating damping instability is caused by the rotating film damping at rotating speeds above a critical value that is less than the flutter speed and a combination instability is caused by the combined effect of film stiffness and damping at rotation speeds above a threshold that is greater than the flutter speed. Also, they showed that the maximum rotation speed of stable disk vibration is bounded above by the lowest onset speed of rotating damping instability. Their analysis showed that the onset speed of the rotating damping instability, for a certain circumferential mode number, exists when the disk speed equals two times the undamped wave speed of the mode in the pre-flutter region.

Naganthan et al. [7] performed a numerical study about the flutter instability of a flexible disk rotating close to a rigid wall. In their study, the disk was modeled using linear plate theory while the flow in the air film was modeled using the classical Reynolds equation of lubrication considering the radial flow. The results from their study showed that the critical speed of a disk rotating close to a rigid wall is increased due to the stiffening effect of the fluid rotating close to the disk. Also, they showed that the rotating disk undergoes flutter instability, and possibly self-excited vibrations, in the presence of air when the speed of rotation is above the critical speed for a given disturbance mode.

Recently, the stabilizer shape and the number of stabilizing pads have been considered [8–11]; in their experimental and numerical studies, they used triangularly arranged stabilizer system and they concluded that this system could effectively stabilize a flexible disk even under conditions with no active stabilizer adjustments (such as axial position control and tilt control) which could not be eliminated at their previous single-stabilizer system.

Kang and Raman [12,13] investigated the vibrations and instability of a rotating disk coupled to acoustic oscillations of surrounding air, theoretically and experimentally. The coupled gyroscopic system equations were formulated using a Kirchhoff plate model for the disk, and the wave equation for the compressible fluid. The analytical study showed that the presence of bulk rotating fluid flow increases the flutter speed for mode coalescence and splits all acoustic-dominated modes into forward and backward traveling waves. From the acoustic pressure measurement, they found that the in-phase and out-of-phase acoustic modes exist in the enclosure. Further, the acoustic modes split into forward and backward traveling waves as the disk rotates. From the vibration measurement of the rotating disk, flutter instability of reflected traveling wave was observed at supercritical speeds. Beyond the flutter speed, it was also observed that acoustic pressures oscillate severely at the frequency of disk instability. Also, they claimed that the flutter instability observed in their experiment is not the mode coalescence but a damping-induced instability leading to the flutter of a single reflected traveling wave.

Because of the low Reynolds number of the fluid film, the earlier studies used the classical Reynolds equation of lubrication to model the flow in the thin air film under the rotating disk. However, the convective inertia forces as well as the coriollis force should be considered when studying the dynamics of disks rotating at reasonably high speeds at which the Reynolds number becomes considerably large. Also, according to Huang and Mote [6], the maximum rotation speed of stable disk vibration is bounded above by the lowest onset speed of rotating damping instability. So, if we try to decrease the rotating damping instability, we can run the flexible disk at high rotation speeds. Practically, it is impossible to remove the rotating damping effect completely, but we can reduce the mean velocity of the rotating damping forces as will be explained in this paper.

The idea of a rotating wall is introduced to decrease the speed of the rotating damping relative to the disk and/or to withstand the propagation of the undamped backward traveling wave through the fluid film by increasing its stiffness and damping capability.

To the best of the authors' knowledge, no attempt was made to study the stability of a flexible disk rotating close to a rigid rotating wall. Also, no attempt was made to consider the effects of inertia and coriollis forces on the dynamics of the disk–fluid system. This may be attributed to the fact that the classical Reynolds equation of lubrication, used in previous works, cannot model these conditions accurately especially when we consider a flexible disk rotating close to a rigid rotating wall.

The present work treats a flexible disk coupled to thin air film and rotating close to a rigid rotating wall. Two new types of flat stabilizers, co-rotating and counter-rotating flat stabilizers, are introduced besides the well-known fixed-plate stabilizer which has been studied extensively. The disk is modeled using linear plate

theory and the air flow between the flexible disk and the rigid wall is modeled using Navier–Stokes and continuity equations. The flow equations are discretized using cell center finite volume method (FVM) and solved numerically with the SIMPLE algorithm. The discretized momentum and continuity equations are solved using ADI method. The spatial terms in the disk model are discretized using finite difference method (FDM) and time integration is performed using fourth-order Runge–Kutta method. The effect of inertia and coriollis forces on the disk displacement and air-film pressure is studied, also the dependence of these forces on the rotation speed, initial gap size and inlet-hole radius is investigated. The developed transient numerical code is used to compare the stability boundaries of the different types of flat stabilizer at a wide range of circumferential mode numbers.

2. Mathematical model

2.1. Flow equations

The model shown in Fig. 1 represents an annular circular disk clamped at its inner radius (r_c), free at its outer radius (r_o) and rotating with constant angular velocity ω above a rigid rotating wall at a distance (h_o). The governing equations for the flow between the rotating flexible disk and the rigid wall are the momentum and continuity equations in cylindrical coordinates (r, θ, z) [14]. The flow in the thin air film is assumed to be steady laminar flow and the fluid is incompressible with constant viscosity. Since the gap height is very small compared with the disk radius, the viscous terms in the order of $(h_o/r_o)^2$ are neglected. The following dimensionless quantities are used to express the flow equations in dimensionless form

$$r^* = \frac{r}{r_o},\ z^* = \frac{z}{h_o},\ v_r^* = \frac{v_r}{v_r^o},\ v_\theta^* = \frac{v_\theta}{v_\theta^o},\ v_z^* = \frac{v_z}{v_z^o},\ p^* = \frac{p}{p_a},\ \mu^* = \frac{\mu}{\mu_{\text{air}}},\ \rho^* = \frac{\rho}{\rho_{\text{air}}}$$

where v_r, v_θ and v_z are the flow velocities along radial, azimuthal and axial coordinates, respectively; ${v_r}^o$, ${v_\theta}^o$ and ${v_z}^o$are reference values for the velocity components. Also, p, μ and ρ are the fluid pressure, fluid viscosity, and fluid density, respectively, while p_a, μ_{air} and ρ_{air} represent the ambient pressure, air viscosity and air density, respectively.

Owing to the vibrations of the flexible disk while rotating close to the rigid wall, the upper boundary of the calculation domain is deformed; hence, a grid mapping to a corresponding computational domain with uniform staggered grids is needed every iteration cycle. In the present study, the physical coordinates (r, θ and z) are mapped into (η, ζ and ξ) coordinates, respectively, in the computational domain. Using the previous assumptions, and after dropping the asterisks, the dimensionless flow equations in the new computational domain considering the convective inertia forces, the fluid coriollis force, the fluid centrifugal force, the fluid viscous forces and the fluid pressure forces, are expressed as

η-momentum equation:

$$Re_r \frac{1}{\eta}\frac{\partial \rho \eta v_r v_r}{\partial \eta} + Re_\theta \frac{1}{\eta}\frac{\partial \rho v_\theta v_r}{\partial \zeta} + Re_z J \frac{\partial \rho v_z v_r}{\partial \xi} - Re_\theta \left(\frac{v_\theta^o}{v_r^o}\right)\frac{\rho v_\theta^2}{\eta} - Re_r J z_\eta \frac{\partial \rho v_r v_r}{\partial \xi}$$
$$- Re_\theta J z_\zeta \frac{1}{\eta}\frac{\partial \rho v_\theta v_r}{\partial \xi} = -\left(\frac{p_a h_o^2}{\mu v_r^o r_o}\right)\left\{\frac{\partial p}{\partial \eta} - J z_\eta \frac{\partial p}{\partial \xi}\right\} + \mu J^2 \frac{\partial^2 v_r}{\partial \xi^2}$$

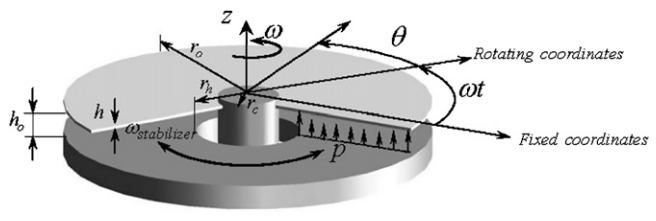

Fig. 1. Analytical model of the disk–fluid system.

ζ-momentum equation:

$$Re_r\frac{1}{\eta}\frac{\partial\rho\eta v_r v_\theta}{\partial\eta}+Re_\theta\frac{1}{\eta}\frac{\partial\rho v_\theta v_\theta}{\partial\zeta}+Re_z J\frac{\partial\rho v_z v_\theta}{\partial\xi}+Re_r\frac{\rho v_r v_\theta}{\eta}-Re_r Jz_\eta\frac{\partial\rho v_r v_\theta}{\partial\xi}$$
$$-Re_\theta Jz_\zeta\frac{1}{\eta}\frac{\partial\rho v_\theta v_\theta}{\partial\xi}=-\left(\frac{p_a h_o^2}{\mu v_\theta^o r_o}\right)\frac{1}{\eta}\left(\frac{\partial p}{\partial\varsigma}-Jz_\varsigma\frac{\partial p}{\partial\xi}\right)\mu J^2\frac{\partial^2 v_\theta}{\partial\xi^2}$$

ξ-momentum equation:

$$Re_r\frac{1}{\eta}\frac{\partial\rho\eta v_r v_z}{\partial\eta}+Re_\theta\frac{1}{\eta}\frac{\partial\rho v_\theta v_z}{\partial\zeta}+Re_z J\frac{\partial\rho v_z v_z}{\partial\xi}-Re_r Jz_\eta\frac{\partial\rho v_r v_\theta}{\partial\xi}$$
$$-Re_\theta Jz_\zeta\frac{1}{\eta}\frac{\partial\rho v_\theta v_z}{\partial\xi}=-\left(\frac{p_a h_o}{\mu v_z^o}\right)J\frac{\partial p}{\partial\xi}+\mu J^2\frac{\partial^2 v_z}{\partial\xi^2}$$

Continuity equation:

$$Re_r\frac{1}{\eta}\frac{\partial\rho\eta v_r}{\partial\eta}+Re_\theta\frac{1}{\eta}\frac{\partial v_\theta}{\partial\zeta}+Re_z J\frac{\partial v_z}{\partial\xi}-Re_r Jz_\eta\frac{\partial\rho v_r}{\partial\xi}-Re_\theta Jz_\zeta\frac{1}{\eta}\frac{\partial\rho v_\theta}{\partial\xi}=0 \tag{1}$$

where Re_r, Re_θ and Re_z are the modified Reynolds numbers along the coordinate directions and J represents the Jacobian of transformation.

The transformation derivatives $\left(z_\eta=\frac{\partial z}{\partial\eta},\ z_\zeta=\frac{\partial z}{\partial\zeta},\ z_\xi=\frac{\partial z}{\partial\xi}\right)$ are calculated numerically using second order central difference approximation for interior grid points and second order forward or backward difference for boundary nodes. An algebraic grid generation technique [15] is used to build up a uniform grid after grid distortion due to disk deformation every iteration cycle.

The dimensionless flow equations when the inertia and the coriollis forces are neglected (inertialess model) can be expressed as

η − momentum equation:

$$-Re_\theta\left(\frac{v_\theta^o}{v_r^o}\right)\frac{\rho v_\theta^2}{\eta}=-\left(\frac{p_a h_o^2}{\mu v_r^o r_o}\right)\left\{\frac{\partial p}{\partial\eta}-Jz_\eta\frac{\partial p}{\partial\xi}\right\}+\mu J^2\frac{\partial^2 v_r}{\partial\xi^2}$$

ζ − momentum equation:

$$Re_r\frac{\rho v_r v_\theta}{\eta}=-\left(\frac{p_a h_o^2}{\mu v_\theta^o r_o}\right)\frac{1}{\eta}\left(\frac{\partial p}{\partial\zeta}-Jz_\zeta\frac{\partial p}{\partial\xi}\right)\mu J^2\frac{\partial^2 v_\theta}{\partial\xi^2}$$

ξ − momentum equation:

$$0=-\left(\frac{p_a h_o}{\mu v_z^o}\right)J\frac{\partial p}{\partial\xi}+\mu J^2\frac{\partial^2 v_z}{\partial\xi^2}$$

Continuity equation:

$$Re_r\frac{1}{\eta}\frac{\partial\rho\eta v_r}{\partial\eta}+Re_\theta\frac{1}{\eta}\frac{\partial v_\theta}{\partial\zeta}+Re_z J\frac{\partial v_z}{\partial\xi}-Re_r Jz_\eta\frac{\partial\rho v_r}{\partial\xi}-Re_\theta Jz_\zeta\frac{1}{\eta}\frac{\partial\rho v_\theta}{\partial\xi}=0 \tag{2}$$

The transformed equations are solved with the following boundary conditions:

- At rigid wall: $z=0$ and $r_h<r\leqslant r_o$, (r_h is the inlet-hole radius)

  $v_r=v_z=0,\ v_\theta=0$ (fixed wall), $v_\theta=\omega r$ (co-rotating wall)
  $v_\theta=-\omega r$ (counter-rotating wall)

- At rotating disk: $z=h_o$ and $r_c\leqslant r\leqslant r_o$

  $v_r=v_z=0,\ v_\theta=\omega r$(no-slip condition)

- At rotating shaft: $r = r_c$ and $0 \leqslant z \leqslant h_o$

$$v_r = v_z = 0,\ v_\theta = \omega r_c$$

- At inlet hole: $z = 0$ and $r_c \leqslant r \leqslant r_h$

$$\frac{\partial v_z}{\partial z} = -\left(\frac{1}{r}\frac{\partial r v_r}{\partial r} + \frac{1}{r}\frac{\partial v_\theta}{\partial \theta}\right)(\text{mass conservation}),\ p = p_a$$

- At outlet: $r = r_o$ and $0 \leqslant z \leqslant h_o$

$$\frac{1}{r}\frac{\partial r v_r}{\partial r} = -\left(\frac{1}{r}\frac{\partial v_\theta}{\partial \theta} + \frac{\partial v_z}{\partial z}\right)(\text{mass conservation})\ \frac{\partial v_\theta}{\partial r} = \frac{\partial v_z}{\partial r} = 0\ (\text{zero gradient}),$$
$$p = p_a$$

- Periodic boundary conditions were used in the circumferential direction as follows:

$$v_r(r,\theta) = v_r(r,\theta+2\pi) \quad v_z(r,\theta) = v_z(r,\theta+2\pi)$$
$$v_\theta(r,\theta) = v_\theta(r,\theta+2\pi) \quad p(r,\theta) = p(r,\theta+2\pi)$$

2.2. Disk equation

Consider the schematic of the flexible disk system shown in Fig. 1. An annular disk of uniform thickness (h) is clamped at radius (r_c) and is free at outer radius (r_o) while rotating with constant angular velocity ω. The disk is thin ($h \ll r_o$) and the disk material is isotropic with Young's modulus (E), Poisson's ratio (υ) and density (ρ_d). The disk material is assumed to be linearly elastic so that Hook's law holds. Also, it is assumed that the in-plane displacements are negligibly small compared with the transverse deflections. As the disk is assumed to be very thin, the transverse deflection is assumed to be constant across the disk thickness. Two coordinate systems are used in the present analysis; the first is rotating with the disk (r, θ, z), while the second coordinate system, used in the fluid equations, is fixed in the space (η, ζ, ξ). The relation between the two coordinate systems is ($\zeta = \theta + \omega t$). Thus, the linear elastic equation describing the small transverse displacement (w) of the thin spinning disk is given by

$$\frac{1}{r}\frac{\partial}{\partial r}\left(r\sigma_r\frac{\partial w}{\partial r}\right) + \frac{1}{r}\frac{\partial}{\partial \theta}\left(\sigma_\theta\frac{1}{r}\frac{\partial w}{\partial \theta}\right) - \frac{D}{h}\nabla^4 w + \frac{p}{h} = \rho_d\frac{\partial^2 w}{\partial t^2} \tag{3}$$

where σ_r and σ_θ are the steady-state stresses in the disk due to the centrifugal action of rotation and are expressed as

$$\sigma_r = \frac{\rho_d\omega^2}{8}\left[(1-\upsilon)(r_c^2 + r_o^2\Gamma) - (3+\upsilon)r^2 + (1-\upsilon)\Gamma\frac{r_c^2 r_o^2}{r^2}\right]$$
$$\sigma_\theta = \frac{\rho_d\omega^2}{8}\left[(1-\upsilon)(r_c^2 + r_o^2\Gamma) - (1+3\upsilon)r^2 - (1-\upsilon)\Gamma\frac{r_c^2 r_o^2}{r^2}\right] \quad \text{and}$$
$$\Gamma = \frac{-(1+\upsilon)r_c^2 + (3+\upsilon)r_o^2}{(1-\upsilon)r_c^2 + (1+\upsilon)r_o^2} \tag{4}$$

In the disk model, (D) represents the bending stiffness of the disk and (p) is the fluid pressure. The boundary conditions for the disk model are; vanishing disk displacement and disk slope at the clamp and vanishing bending moment and shear force at the outer radius. Also, periodic boundary condition is used, in the circumferential direction, for the disk displacement and disk axial velocity. The same disk model was assumed

by Hosaka and Crandall [3] and Naganathan et al. [7]. In the present analysis, the disk equation was expressed in dimensionless form using appropriate parameters.

3. Numerical method

3.1. Fluid equations

The fluid equations are discretized using cell-centered FVM on a uniform staggered grid. The pressure values are stored at the cell centers while the velocity values are stored at the cell boundaries. The radial, azimuthal and axial momentum equations are integrated over v_r, v_θ and v_z cells, respectively, while the continuity equation is integrated over p cell. Gauss's divergence theorem is used to transform the volume integral over the cell into a surface integral over the cell boundary. The velocities at cell boundaries are approximated using the UPWIND differencing scheme. Because of the staggered grid pattern, six grid notations (I, i, J, j, K, k) are used to describe the velocity and pressure locations. The upper case letters are used for indexing the pressure nodes while lower and upper case letters are used for indexing the velocity components. The discretized flow equations are solved with the semi-implicit method for pressure linked equations (SIMPLE) algorithm, Patankar [16], using the ADI method with TDMA. It is well known that the pressure correction equation is susceptible to divergence unless some under-relaxation is used. For this reason, under-relaxation factors are used for the air velocity components and air-film pressure.

3.2. Disk equation

The spatial terms in the disk equation are discretized using second order FDM. The discretized equation can be expressed as

$$\begin{aligned}\frac{\partial^2 w}{\partial t^2} = {} & C_1 w_{i,j} + C_2 w_{i-1,j+1} + C_3 w_{i,j+1} + C_4 w_{i+1,j+1} + C_5 w_{i+1,j} + C_6 w_{i+1,j-1} + C_7 w_{i,j-1} \\ & + C_8 w_{i-1,j-1} + C_9 w_{i-1,j} + C_{10} w_{i,j+2} + C_{11} w_{i+2,j} + C_{12} w_{i,j-2} \\ & + C_{13} w_{i-2,j} + \text{pressure term}\end{aligned} \tag{5}$$

The coefficients $C_1 \sim C_{13}$ aroused from the discretization process while the pressure term is the source term in the disk equation. The temporal derivative in the disk equation is integrated using fourth-order Runge–Kutta time marching scheme. Since the discretized disk equation is second order in time, it is reduced to a set of two first-order equations expressed as

$$\frac{\partial v_{i,j}}{\partial t} = f_1(t, w_{i,j}, v_{i,j}), \quad \frac{\partial w_{i,j}}{\partial t} = f_2(t, w_{i,j}, v_{i,j}) \tag{6}$$

where $v_{i,\,j}$ represents the velocity at the nodal point (i, j). The evolution of the coupled fluid–disk system is simulated according to the flow chart shown in Fig. 2. In the problem simulation, two convergence criteria are used (convergence criteria 1 and 2, shown in the flow chart). The first one is for the continuity residual which is chosen to be less than 0.0001 for convergence. The second is for the pressure change under the rotating disk and is chosen to be less than some specified value ($\varepsilon \cong 10^{-6}$) where the condition for convergence is

$$\frac{\sum_{i=1}^{NI}\sum_{j=1}^{NJ}(p_{i,j}^{\text{new}} - p_{i,j}^{\text{old}})}{\sum_{i=1}^{NI}\sum_{j=1}^{NJ}(p_{i,j}^{\text{new}})} \leqslant \varepsilon \tag{7}$$

In this numerical simulation, the pressure obtained from the iterative solution of the flow equations is used to calculate the disk displacement at the next time step. Then, the boundary conditions for the flow equations are updated and a numerical grid generation technique is used with the SIMPLE algorithm to calculate the new pressure field to be used for the next iteration cycle in disk equation. The process is repeated until the disk reaches a steady-state deflection determined by convergence criterion 2.

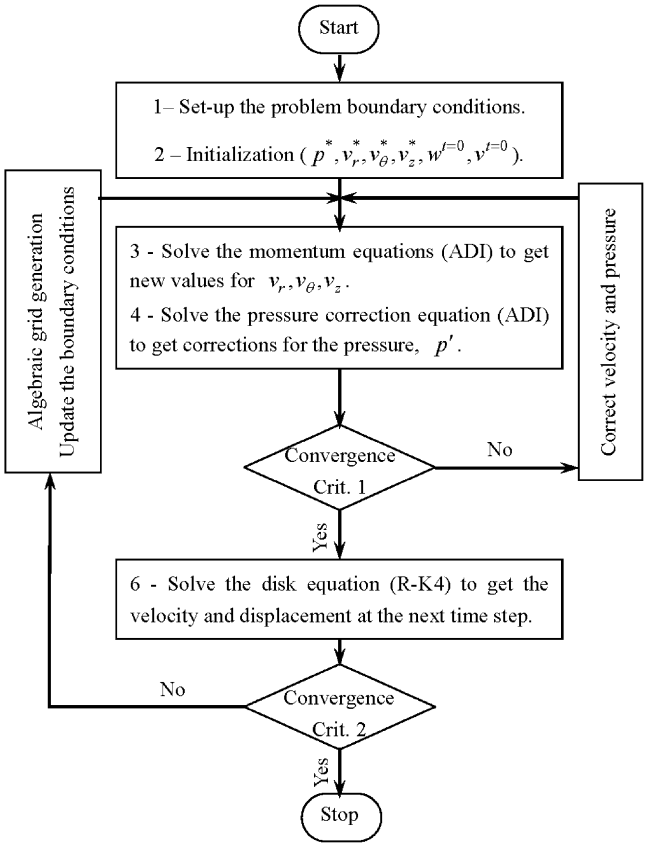

Fig. 2. Flow chart of the present numerical simulations.

Table 1
Specifications of the polycarbonate flexible disk

Outside radius (r_0) (mm)	Clamping radius (r_c) (mm)	Thickness (h) (mm)	Density (ρ_d) ($\mathrm{kg\,m^{-3}}$)	Elasticity modulus (E) (GPa)	Poisson's ratio (ν)
60	12.5	0.095	1200	2.5	0.23

4. Numerical results

Through out the present investigations, a polycarbonate flexible disk with the specifications given in Table 1 is used. Also, the properties of air in the gap between the disk and the rigid wall are $\rho_{\mathrm{air}} = 1.23\,\mathrm{kg\,m^{-3}}$, $\mu_{\mathrm{air}} = 17.9 \times 10^{-6}\,\mathrm{Pa\,s}$ and $p_a = 10^5\,\mathrm{N\,m^{-2}}$. Due to the geometry of the problem and the constraints imposed on the dimensions of the fluid control volume, a fine-grid mesh has to be used to avoid the divergence of the SIMPLE algorithm. In the present analysis, the number of grid points in the radial direction is chosen to be 160 so as not to affect the pressure in the air film at high rotation speeds. In the axial direction, the number of grid points is 6 while the number of grid points in the circumferential direction depends on the mode number. In the following results, eight grid points are used to catch one wavelength of the harmonic mode. Due to this fine-grid mesh, the time step for the present analysis is in the order of 0.1 μs. However, the nonlinearity of the introduced equations and the small time step increases the computation time considerably.

The present numerical investigations are carried out through three stages. For the first stage, the effects of fluid inertia forces as well as the fluid coriollis force on the disk displacement and air-film pressure are investigated through a comparison between the results obtained from the complete mathematical model (given

by Eq. (1)) and that obtained from the inertialess model (given by Eq. (2)). In the second stage, the steady-state behavior of the disk using the inertia model, given by Eq. (1), is determined and the effects of the rotation speed, the inlet-hole radius and the initial gap size on the steady-state disk deflection, steady-state film pressure, steady-state inlet axial-velocity and steady-state outlet radial-velocity are investigated. In the third stage, the steady-state disk displacement and the steady-state air-film pressure are used as initial conditions for the transient numerical simulations, and then the later is used to determine a bound for the critical speed at a wide range of circumferential mode numbers for the different types of stabilizer.

4.1. Fluid inertia effects

In the steady-state analysis, the spatial terms in the disk equation are discretized using second-order FDM and solved numerically using Gauss's Point over-relaxation method. Fig. 3 shows a comparison between the steady-state disk displacement as well as air-film pressure obtained with the mathematical model considering fluid inertia (Eq. (1)) and those obtained with the inertialess model (Eq. (2)) at different disk rotation speeds. It is important to mention that the stabilizer was assumed to be fixed for the results presented in this section. It is noticeable from Fig. 3 that the difference between the two models increases as the disk rotation speed increases. Thus, it can be concluded that the effect of the fluid inertia forces on the disk displacement becomes more pronounced as the disk rotation speed increases. Also, Fig. 4 shows a comparison between the steady-state disk displacement and air-film pressure obtained with inertia model and those obtained with the inertialess model at different initial gap sizes. It is clear from Fig. 4 that the inertia forces affect the disk displacement only when the initial gap size is comparatively large. Also, a comparison between the steady-state disk displacement and air-film pressure obtained with inertia model and those obtained with the inertialess model at different inlet-hole radii is shown in Fig. 5. It can be noticed from Fig. 5 that the inertia forces are almost independent of the inlet-hole radius (r_h) as the difference between the two models is approximately the same at the different inlet-hole radii. Thus, it can be concluded from Figs. 3 to 5 that the fluid inertia forces and fluid coriollis force become more effective and should be considered in future simulations whenever the flexible disk spins with high rotation speeds over a rigid stabilizer where the gap in-between is comparatively large.

4.2. Steady-state analysis

For the above reasons, the results presented in following sections are obtained with the mathematical model given by Eq. (1) considering fluid inertia and coriollis forces in order to accurately simulate the dynamics of the fluid–disk system.

It is well known that the disk rotation generates a centrifugal force on the gas molecules that acts to drive the molecules outwards. So, a negative pressure is generated in the gas film to balance the centrifugal force. This negative pressure pulls the disk downwards until the negative pressure force (F_P) is balanced by the

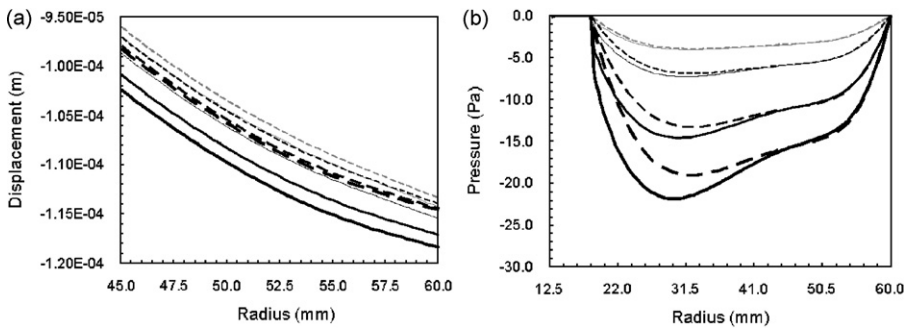

Fig. 3. Rotation speed effect ($h_o = 200\,\mu m$, $r_h = 18.77\,mm$): (a) Steady-state disk displacement. (b) Steady-state air film pressure. —— 5400 rev min^{-1} ---- 5400 rev min^{-1} (inertialess) — 7200 rev min^{-1} ---- 7200 rev min^{-1} (inertialess) — 10,000 rev min^{-1} --- 10,000 rev min^{-1} (inertialess) ▬▬ 12,000 rev min^{-1} ▬ ▬ 12,000 rev min^{-1} (inertialess).

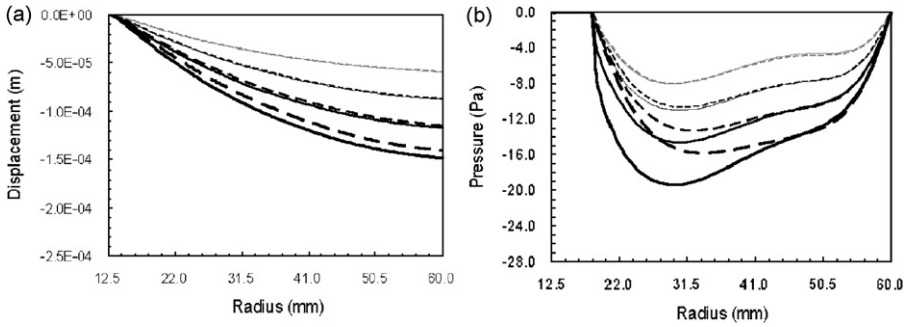

Fig. 4. Initial gap-size effect, ($\omega = 10{,}000\,\mathrm{rev\,min^{-1}}$, $r_h = 18.77\,\mathrm{mm}$): (a) Steady-state disk displacement. (b) Steady-state air film pressure. —— 0.1 mm - - - - 0.1 mm (inertialess) — 0.15 mm ---- 0.15 mm (inertialess) — 0.2 mm --- 0.2 mm (inertialess) ▬▬ 0.25 mm ▬ ▬ 0.25 mm (inertialess).

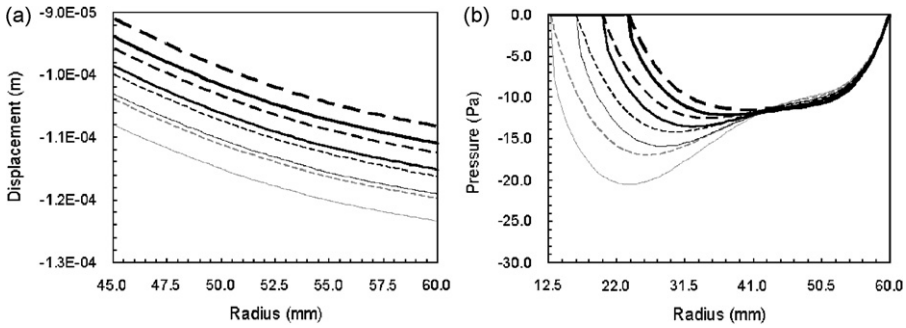

Fig. 5. Inlet-hole radius effect, ($\omega = 10{,}000\,\mathrm{rev\,min^{-1}}$, $h_o = 200\,\mu\mathrm{m}$): (a) Steady-state disk displacement. (b) Steady-state air film pressure. —— 13.10 mm - - - - 13.10 mm (inertialess) — 16.68 mm ---- 16.68 mm (inertialess) — 20.27 mm --- 20.27 mm (inertialess) ▬▬ 23.85 mm ▬ ▬ 23.85 mm (inertialess).

centrifugal forces acting on the disk material (F_C), the membrane forces associated with stresses in the disk (F_S) and the disk resistance to bending (F_B). When these forces are in balance, the disk reaches an axisymmetric steady-state displacement (hat shape [1]).

The effect of increasing rotation speed on the steady-state disk deflection, air-film pressure and inlet axial velocity for the three types of stabilizer is shown in Fig. 6. The figure shows that the negative pressure in the air film increases as the disk rotation speed increases while the disk deflection does not affected much. This is because the increase in the negative pressure force (F_P) is accompanied by a corresponding increase in the resisting disk-material forces (F_C and F_S); thus the disk displacement is not affected much. Also, it can be read from the figure that increasing rotation speed increases the outlet mass flow rate which is compensated by a corresponding increase in the inlet flow rate as shown from the increase in the inlet axial velocity. Also, it is noticeable from Fig. 6 that the flexible disk rotating close to a counter-rotating stabilizer has the smallest deflection relative to the other two types. The inlet-hole radius effect on the steady-state disk deflection and steady-state outlet radial velocity, for the three types of stabilizer, is shown in Fig. 7. The dimensionless gap shown in Fig. 7 represents the axial distance normalized with the tip point displacement. It can be noticed from Fig. 7 that the decrease of the inlet-hole radius is accompanied by the increase of the flexible disk deflection. The reason for that is the increase of the film negative pressure due to the continuous outward flow without a sufficient compensation from the inlet hole. The effect of initial gap height h_o on the disk deflection is shown in Fig. 8. Increasing the gap height reduces the shear resistance to the outward flow, thus increases the outward flow rate and consequently increases the film negative pressure causing the disk to deflect more towards the stabilizer.

The most important result from the steady-state analysis is that the flexible disk rotating close to a counter-rotating flat stabilizer has the smallest deflection relative to the other two types of stabilizer. The reason for

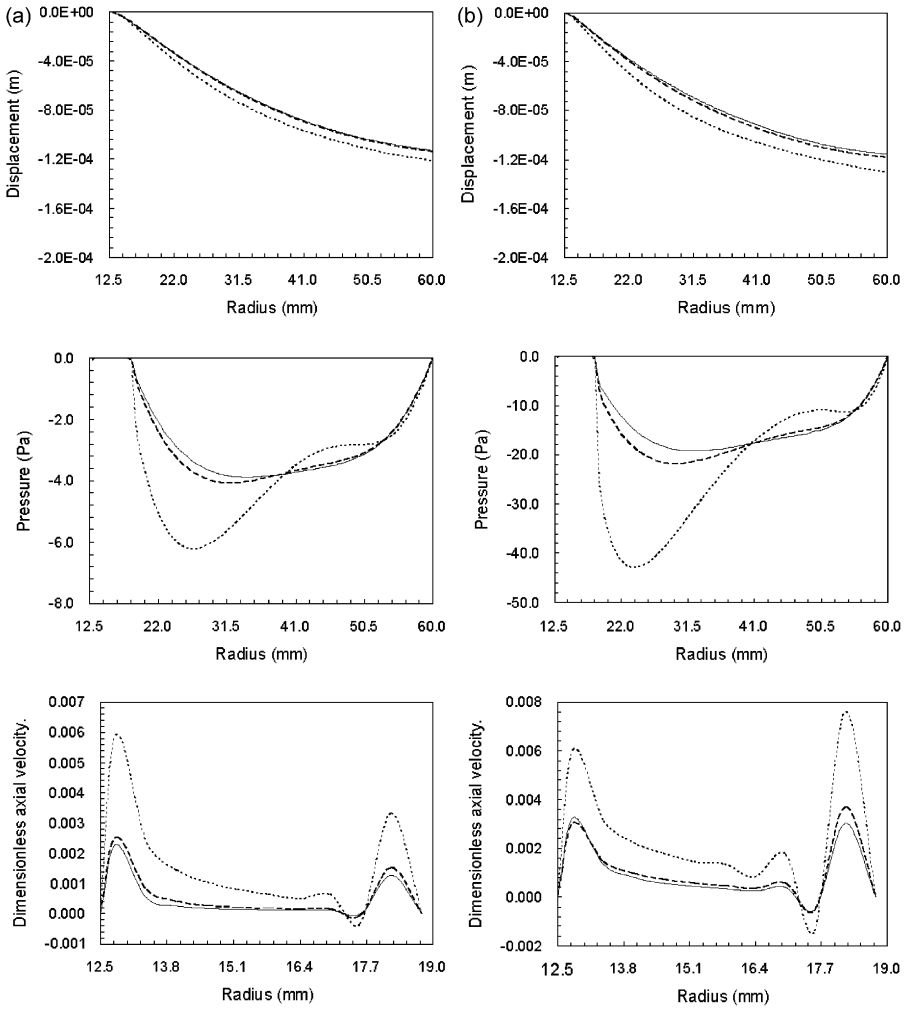

Fig. 6. Disk deflection, pressure distribution and inlet axial velocity (v_z) variations in radial direction ($h_o = 200\,\mu m$, $r_h = 18.77\,mm$): (a) $\omega = 5400\,rev\,min^{-1}$. (b) $\omega = 12{,}000\,rev\,min^{-1}$. — Counter rotating stabilizer ---- Fixed stabilizer ..... Co-rotating stabilizer.

that is the smallest outward flow and consequently, the smallest negative pressure generated in the air film. This result can be explained as follows: Introducing the counter rotating stabilizer reduces the effect of the centrifugal force acting on the air molecules by creating a high shear plane, in the gap between the rotating disk and the counter rotating stabilizer, which in turn increases the resistance for the outward flow.

4.3. Transient numerical simulation

The objective of developed transient numerical code is to trace a bound for the velocity at which the onset of rotating damping instability occurs for the three types of flat stabilizers. This is achieved by increasing the disk rotation speed at a constant circumferential mode number and checking the stability of the steady-state disk–fluid system.

According to Yasuda et al. [5], any disturbance on a rotating disk propagates as a combination of forward and backward traveling waves. Also they showed that the forward traveling wave always decays while the behavior of the backward traveling wave depends on its frequency as well as the damping and lifting components of the air film, C_D and C_L, respectively. At speeds of rotation lower than the critical speed, the real part of all eigenvalues are negative and thus, the forward and backward traveling waves decay

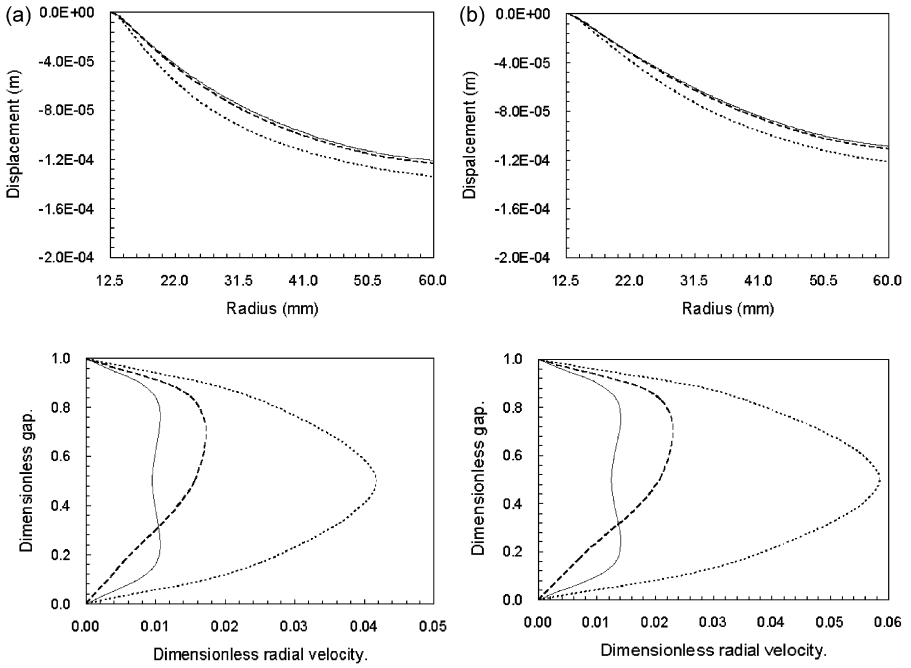

Fig. 7. Disk deflection and outlet radial velocity (v_r) at two different inlet-hole radii (r_h). ($\omega = 10{,}000\,\mathrm{rev\,min^{-1}}$, $h_o = 200\,\mu\mathrm{m}$): (a) $r_h = 13.1\,\mathrm{mm}$. (b) $r_h = 23.85\,\mathrm{mm}$. — Counter rotating stabilizer ---- Fixed stabilizer ..... Co-rotating stabilizer.

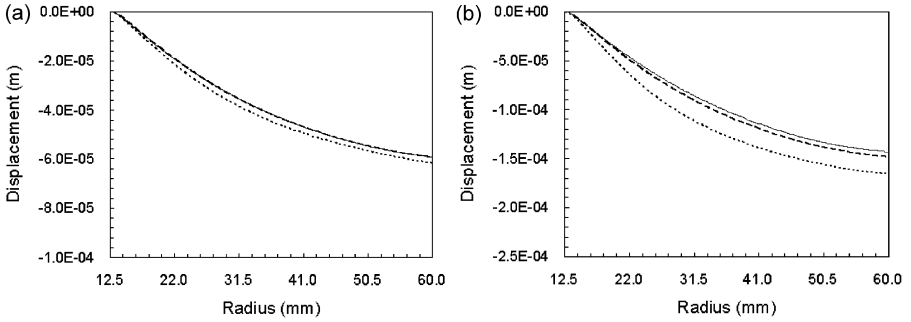

Fig. 8. Disk deflection at two different gap sizes (h_o), $\omega = 10{,}000\,\mathrm{rev\,min^{-1}}$, $r_h = 18.77\,\mathrm{mm}$: (a) $h_o = 100\,\mu\mathrm{m}$. (b) $h_o = 250\,\mu\mathrm{m}$ — Counter rotating stabilizer ---- Fixed stabilizer ..... Co-rotating stabilizer.

exponentially with time and the disk reaches an equilibrium steady state which is mostly the axisymmetric steady-state solution. At the critical speed, the real part of one eigenvalue is zero while all the other eigenvalues have negative real parts. Thus, the corresponding wavenumber of the backward traveling wave does not grow or decay in time for the linear model. However, for the forward traveling wave, the real part of the eigenvalue is still negative, thus the forward traveling waves die down with time. When the speed of rotation of the disk is above the critical speed for a given wavenumber, the real part of the corresponding eigenvalue for the backward traveling wave is positive. The forward traveling waves decay in amplitude with time, while the supercritical backward traveling wave increases in amplitude with time. Thus, it is the supercritical backward traveling wave that leads to self-excited oscillations in the fluid–disk system.

In the following results, the steady-state disk displacement is perturbed by a small non-axisymmetric component and given as initial condition for the transient analysis while the pressure initial condition is assumed to be the steady-state pressure field. Also the initial value for the axial velocity of the disk is assumed

to be zero. The initial conditions for the transient analysis are as follows:

$$w(r,\theta,t=0) = w_o(r)(1+\varepsilon \sin m\theta)$$
$$p(r,\theta,t=0) = p_o(r)$$
$$v(r,\theta,t=0) = 0 \tag{8}$$

where m represents the mode number. Also, w_o and p_o represent the steady-state disk displacement and steady-state film pressure, respectively. It is important to mention that the value of the perturbation parameter (ε) is set to 0.01. Several cases have been studied in order to determine a bound for the critical speed at the considered mode number. At a given mode number, the rotation speed is increased with an increment of 500 rev min^{-1} and the evolution of the fluid–disk system with time is investigated.

The variation of the disk displacement with time at a point and the disk deflection shape before divergence when the disk rotates close to a counter rotating stabilizer and the mode number of the initial disturbance is 10 is shown in Fig. 9. It is clear from Fig. 9(a) that the initial disturbance dies out and eventually the disk converges to the steady-state displacement when the disk rotates at 15,500 rev min^{-1} while Fig. 9(b) shows that the initial disturbance builds-up and the same disk experiences self-excited vibrations when it rotates at 16,000 rev min^{-1}. Also, this result is in a good agreement with the results obtained by Hosaka and Crandall [3] that the disk displacements are only large near the outer edge. The results from Fig. 9 suggest that the critical speed of rotating damping instability when the disk rotates close to a counter rotating stabilizer is somewhere between 15,500 and 16,000 rev min^{-1} if the mode number of the initial disturbance is 10.

Fig. 10 shows the variation of the disk displacement with time at a point and the disk deflection shape before divergence when the disk rotates close to a fixed stabilizer and the mode number of the initial disturbance is 10. It can be deduced from the figure that the critical speed when the disk rotates close to a fixed stabilizer is somewhere between 12,000 and 12,500 rev min^{-1}.

Fig. 11 suggests that the critical speed of rotating damping instability when the disk rotates close to a co-rotating stabilizer is somewhere between 6300 and 6500 rev min^{-1}. Thus, the results from the transient numerical simulations, when the mode number is 10, show that the highest critical speed can be obtained when the flexible disk rotates close to a counter rotating stabilizer.

According to [3,5], these results can be interpreted as follows; when using co-rotating stabilizer, the mean flow velocity is same as the disk speed, so that the rotating damping energizes all mode numbers of the undamped wave, because their speed certainly is lower than the disk speed. For the fixed stabilizer, the rotating damping speed is the mean velocity of the circumferential flow which is a half of the disk speed and hence, the rotating damping instability occurs only when the speed of the backward traveling wave is less than half the disk speed. However, the results showed that the behavior of the flexible disk when rotating close to a

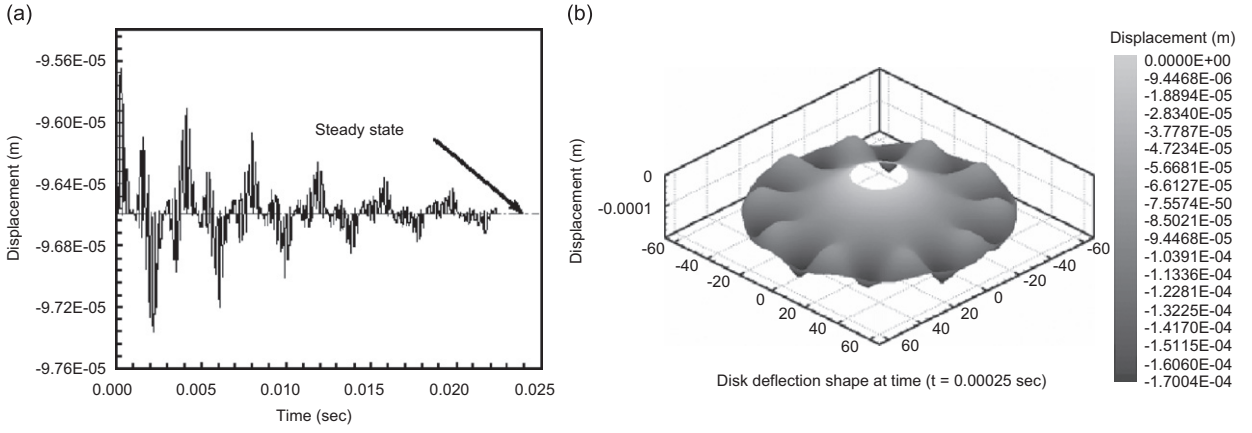

Fig. 9. System evolution with counter rotating stabilizer ($m = 10$, $h_o = 200\,\mu$m, $r_h = 17.88$ mm): (a) Point displacement with time ($\omega = 15{,}500$ rev min^{-1}/$r = 42$ mm, $\theta = 28^\circ$). (b) Disk displacement before divergence ($\omega = 16{,}000$ rev min^{-1}/$t = 0.00025$ s).

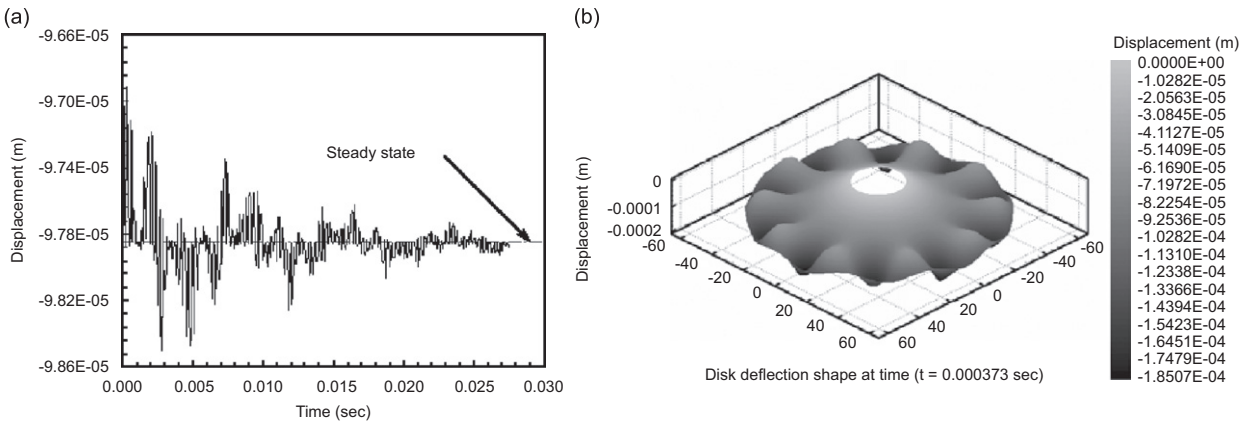

Fig. 10. System evolution with fixed stabilizer, ($m = 10$, $h_o = 200\,\mu m$, $r_h = 17.88\,mm$): (a) Point displacement with time ($\omega = 12{,}000\,rev\,min^{-1}/r = 42\,mm$, $\theta = 28^\circ$). (b) Disk displacement before divergence ($\omega = 12{,}500\,rev\,min^{-1}/t = 0.000373\,s$).

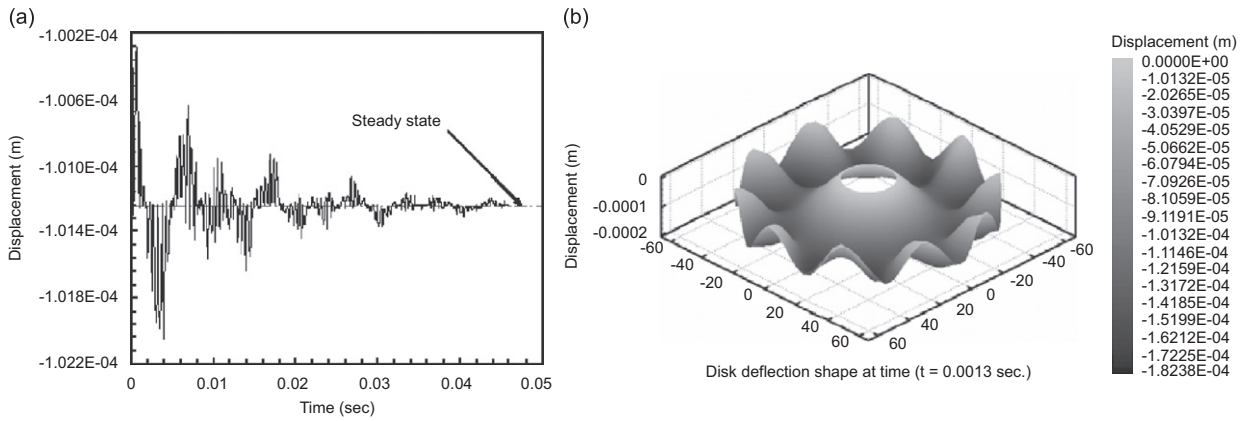

Fig. 11. System evolution with co-rotating stabilizer ($m = 10$, $h_o = 200\,\mu m$, $r_h = 17.88\,mm$): (a) Point displacement with time ($\omega = 6300\,rev\,min^{-1}/r = 42\,mm$, $\theta = 28^\circ$). (b) Disk displacement before divergence ($\omega = 6500\,rev\,min^{-1}/t = 0.0013\,s$).

counter-rotating stabilizer with initial gap of h_o is analogous to that when rotating close to a fixed stabilizer with initial gap of $0.5h_o$.

From the fluid dynamics point of view; using a counter rotating stabilizer divides the air film in the gap between the disk and the stabilizer into two zones, each one rotates with the adjacent wall, with a high shear plane in-between. This fluid–structure system increases the damping capability of the air film and resists the propagation of the initial disturbance in the air-film layers and thereby opposes the propagation of the undamped wave allowing the disk to rotate stably at high rotation speeds. The results showed clearly that it is possible to have a stable disk at high rotation speeds and with two-times larger initial-gap when using counter-rotating stabilizer instead of the fixed flat stabilizer.

Fig. 12 shows the pressure variation with time at a point under the disk and the pressure field under the disk before divergence when the flexible disk rotates close to a fixed stabilizer and the mode number of the initial disturbance is 20. The figure shows that the air-film damps out the initial disturbance when the rotation speed is $11{,}500\,rev\,min^{-1}$ while it excites the backward traveling wave when the disk rotates at $12{,}000\,rev\,min^{-1}$. With a similar manner, the air film behaves when the disk rotates close to a counter rotating stabilizer at 14,500 and $15{,}000\,rev\,min^{-1}$, respectively, as shown in Fig. 13. The most noticeable result from Figs. 12 and 13 is that the pressure field under the disk before divergence in both cases is very similar.

The velocity field in the air film at an angle ($\theta = 2.25^\circ$), before disk divergence, when using fixed stabilizer and counter rotating stabilizer is shown in Fig. 14. The figure shows clearly that the profile of the velocity field

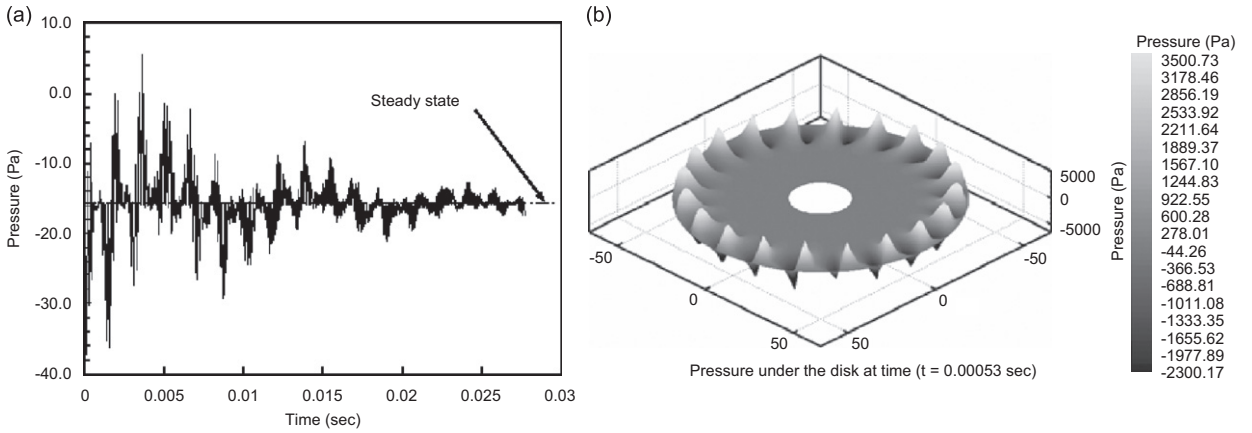

Fig. 12. Air film pressure when using fixed stabilizer ($m = 20$, $h_o = 200\,\mu m$, $r_h = 17.88\,mm$): (a) Pressure variation with time ($\omega = 11{,}500\,rev\,min^{-1}/r = 42\,mm$, $\theta = 15.75^\circ$). (b) Air film pressure before divergence ($\omega = 12{,}000\,rev\,min^{-1}/t = 0.00053\,s$).

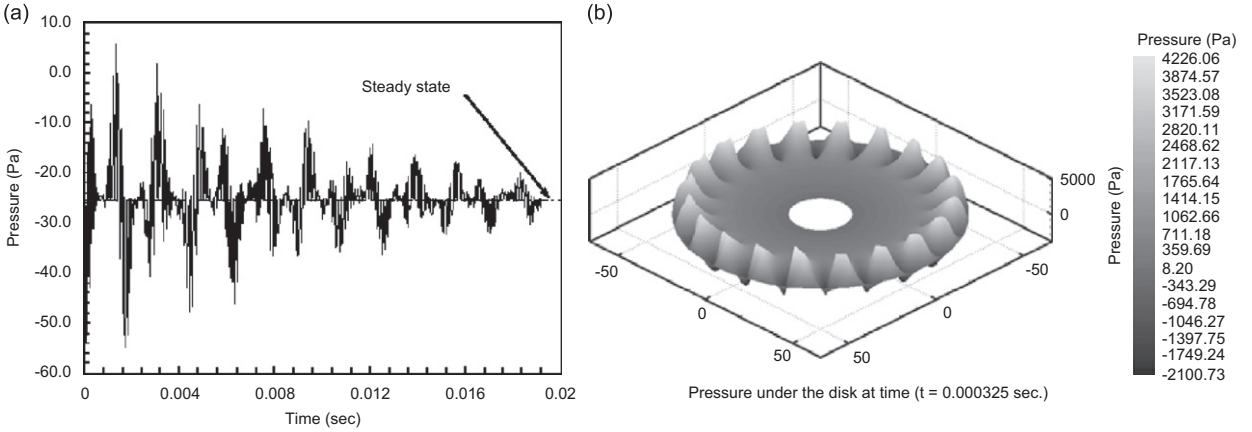

Fig. 13. Air film pressure using counter rotating stabilizer ($m = 20$, $h_o = 200\,\mu m$, $r_h = 17.88\,mm$): (a) Pressure variation with time ($\omega = 14{,}500\,rev\,min^{-1}/r = 42\,mm$, $\theta = 15.75^\circ$). (b) Air film pressure before divergence ($\omega = 15{,}000\,rev\,min^{-1}/t = 0.000325\,s$).

near the rotating disk when using counter rotating stabilizer is very similar to that when using fixed stabilizer. In other words, if the velocity field under the flexible disk rotating close to a counter rotating stabilizer (Fig. 14b) was divide into two halves, the upper half will be very similar to the velocity profile when the flexible disk rotating close to a fixed stabilizer (Fig. 14a). This result supports our suggestion that the behavior of the flexible disk rotating close to a counter rotating stabilizer with initial gap of h_o is analogous to that when rotating close to a fixed stabilizer with a gap of $0.5h_o$.

In a similar manner, the transient numerical simulation is utilized to determine the bounds for the critical speeds at a wide range of mode numbers, from 5 to 30, as shown in Fig. 15. For these bounds, the lower value gives the disk rotation speed where the mode is stable and the upper value gives a speed for which the disk is unstable.

Fig. 15 shows that the critical speed of rotating damping instability when the disk rotates close to a counter rotating stabilizer is higher than that when rotating close to the other two types of stabilizer for all mode numbers. Also, it is clear that the critical speed decreases when the mode number increases and the critical speed decreases sluggishly when using co-rotating stabilizer.

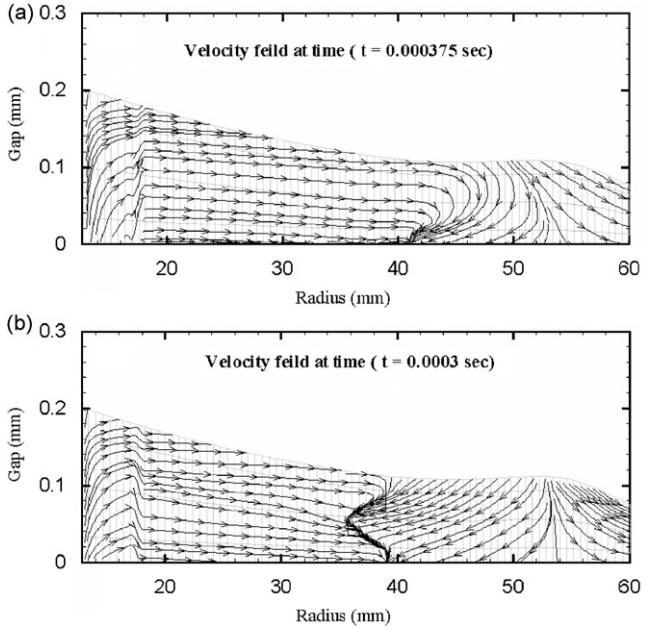

Fig. 14. Velocity field before divergence at ($\theta = 2.25°$): (a) With fixed stabilizer ($m = 20$, $\omega = 12{,}000\,\text{rev min}^{-1}$, $h_o = 200\,\mu\text{m}$, $r_h = 17.88\,\text{mm}$) (b) With counter rotating stabilizer ($m = 20$, $\omega = 15{,}000\,\text{rev min}^{-1}$, $h_o = 200\,\mu\text{m}$, $r_h = 17.88\,\text{mm}$).

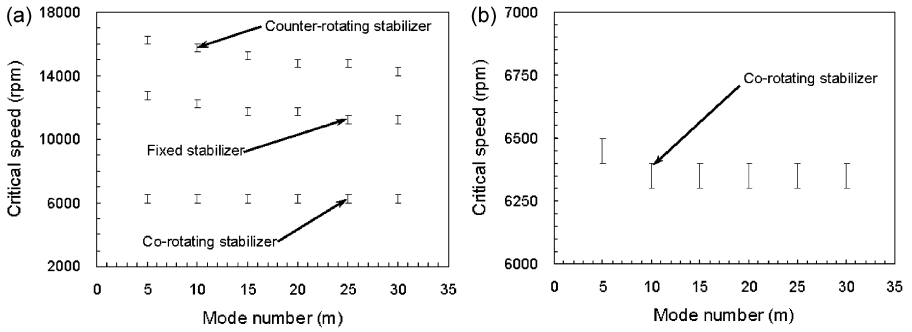

Fig. 15. Critical speed of rotating damping instability as a function of the mode number for the three types of stabilizer at ($h_o = 200\,\mu\text{m}$, $r_h = 17.88\,\text{mm}$).

5. Conclusions

The following conclusions can be drawn out from the present analysis:

- The fluid inertia forces and fluid coriollis force becomes more effective and should be considered in future simulations whenever the flexible disk spins with high rotation speeds over a rigid stabilizer where the gap in-between is comparatively large.
- Increasing disk rotation speed has a very small effect on the disk deflection compared with the effects of increasing the initial gap height or increasing the inlet-hole radius.
- The flexible disk rotating close to a counter-rotating flat stabilizer has the smallest deflection relative to the other two types of stabilizer.
- Using co-rotating stabilizer, the air film can excite all undamped traveling waves causing rotating damping instability while using fixed stabilizer can excite these waves only at certain speeds.

- The onset speed of rotating damping instability can be increased by introducing a counter-rotating flat stabilizer instead of the well-known fixed stabilizer.
- The behavior of the flexible disk rotating close to a counter rotating stabilizer with an initial gap of h_o is analogous to that when rotating close to a fixed stabilizer with an initial gap of $0.5h_o$.

Acknowledgments

This work was supported by the Korea Research Foundation; grant funded by the Korea Government (MOEHRD) (KRF-2006-211-D00013). The authors would like to thank the KRF for the financial support of this research.

References

[1] I. Pelech, A.H. Shapiro, Flexible disk rotating on a gas film next to a wall, *Journal of Applied Mechanics—Transactions of the ASME* 31 (1964) 577–584.
[2] D.B. Bogy, F.E. Talke, Steady axisymmetric solutions for pressurized rotating flexible disk packs, *IBM Journal of Research Development* 22 (2) (1978) 179–184.
[3] H. Hosaka, S.H. Crandall, Self-excited vibrations of a flexible disk rotating on an air film above a flat surface, *Acta Mechanica (Supplement)* 3 (1992) 115–127.
[4] C. D'Angelo III, C.D. Mote, Aerodynamically excited vibration and flutter of a thin disk rotating at supercritical speed, *Journal of Sound and Vibration* 168 (1) (1993) 15–30.
[5] K. Yasuda, T. Torii, T. Shimizu, Self-excited oscillations of a circular disk rotating in air, *JSME International Journal* 35 (3) (1992) 347–352 series III.
[6] F.Y. Huang, C.D. Mote, On the instability mechanisms of a disk rotating close to a rigid surface, *Journal of Applied Mechanics—Transactions of the ASME* 62 (1995) 764–771.
[7] G. Naganathan, S. Ramadhayani, A.K. Bajaj, Numerical simulations of flutter instability of a flexible disk rotating close to a rigid wall, *Journal of Vibration and Control* 9 (2003) 95–118.
[8] Aman Yasutomo, Onagi Nobuaki, Murata Shozo, Uchida Keisuke, Effect of stabilizer in reducing effects of axial runout on a flexible optical disk, *Japanese Journal of Applied Physics* 43 (7B) (2004) 4835–4838.
[9] Aman Yasutomo, Onagi Nobuaki, Murata Shozo, Uchida Keisuke, Aerodynamic stabilization of flexible optical disk with triangularly arranged stabilizer system, *Japanese Journal of Applied Physics* 44 (5B) (2005) 3487–3492.
[10] Onagi Nobuaki, Aman Yasutomo, Murata Shozo, Uchida Keisuke, High-density recording on air-stabilized flexible optical disk, *Japanese Journal of Applied Physics* 43 (7B) (2004) 5009–5013.
[11] Aman Yasutomo, Onagi Nobuaki, Uchida Keisuke, Aerodynamic stabilization of a flexible optical disk with an asymmetrically and triangularly arranged stabilizer, *Microsystem Technologies* 13 (2007) 1055–1062.
[12] Kang Namcheol, Raman Arvind, Vibrations and stability of a flexible disk rotating in a gas-filled enclosure—part 1: theoretical study, *Journal of Sound and Vibration* 296 (2006) 651–675.
[13] Kang Namcheol, Raman Arvind, Vibrations and stability of a flexible disk rotating in a gas-filled enclosure—part 2: experimental study, *Journal of Sound and Vibration* 296 (2006) 676–689.
[14] Bernard J. Hamrock, *Fundamentals of Fluid Film Lubrication*, McGraw-Hill, New York, 1994.
[15] Klaus A. Hoffmann, Steve T. Chiang, *Computational Fluid Dynamics for Engineers*, Engineering Education System, Wichita, KS, USA, 1995.
[16] S.V. Patankar, *Numerical Heat Transfer and Fluid Flow*, Hemisphere Publishing Corporation, Taylor & Francis Group, New York, 1980.